Inertial waves in turbine rim seal flows

Feng Gao (高锋) ⓘ,[*] John W. Chew,[†] and Olaf Marxen[‡]

Faculty of Engineering and Physical Sciences, University of Surrey, Guildford GU2 7XH, United Kingdom

Rotating fluids are well-known to be susceptible to waves. This has received much attention from the geophysics, oceanographic and atmospheric research communities. Inertial waves, which are driven by restoring forces, for example, the Coriolis force, have been detected in the research fields mentioned above. This paper investigates inertial waves in turbine rim seal flows in turbomachinery. These are associated with the large-scale unsteady flow structures having distinct frequencies, unrelated to the main annulus blading, identified in many experimental and numerical studies. These unsteady flow structures have been shown in some cases to reduce sealing effectiveness and are difficult to predict with conventional steady Reynolds-averaged Navier-Stokes (RANS) approaches. Improved understanding of the underlying flow mechanisms and how these could be controlled is needed to improve the efficiency and stability of gas turbines. This study presents large-eddy simulations for three rim seal configurations—chute, axial, and radial rim seals—representative of those used in gas turbines. Evidence of inertial waves is shown in the axial and chute seals, with characteristic wave frequencies limited within the threshold for inertial waves given by classic linear theory (i.e., $|f^*/f_{\rm rel}| \leqslant 2$) and instantaneous flow fields showing helical characteristics. The radial seal, which limits the radial fluid motion with the seal geometry, restricts the Coriolis force and suppresses the inertial wave.

I. INTRODUCTION

Rotating fluids exist in many areas, including geophysics, oceanography, atmospherics, and engineering applications such as turbomachinery [1]. Such flows are known to be susceptible to waves, as illustrated by Andereck *et al.* [2] in a study of flow regimes in co-centric differentially rotating cylinders. A wide variety of waveforms were observed by fixing the angular speed of the outer cylinder and gradually increasing the angular speed of the inner cylinder. These include, for example, classic and turbulent Taylor vortices and further spiral interpenetrating, modulated, and wavy flows. Inertial waves, which can be demonstrated mathematically from the inviscid linearized Navier-Stokes equations in a rotating frame of reference, have been detected in the Earth's fluid core [3,4], the atmosphere [5], the ocean [6,7] and some laboratory experiments [8–10]. Wave-like large-scale unsteady flow structures with intrinsic frequencies unrelated to the main annulus blading are also observed in turbine rim seal flows, as reported in a review paper by Chew *et al.* [11], but the driving mechanisms are not yet clearly understood.

In axial gas turbines gas is energized through compression and combustion processes prior to generating work through the turbine stages. The gas temperature can exceed the metal's melting point. As a consequence, cooling air, diverted from the compressor, must be used to keep the hot

————————

[*]Corresponding author: f.gao@surrey.ac.uk

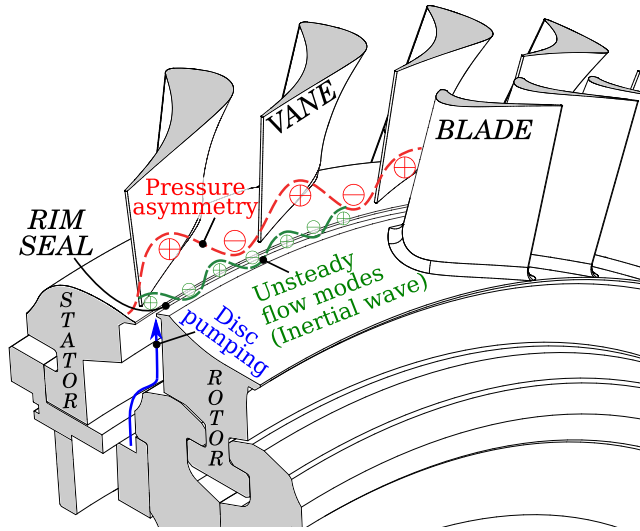[†]j.chew@surrey.ac.uk

[‡]o.marxen@surrey.ac.uk

FIG. 1. Illustration of a typical rim seal configuration in an axial turbine stage and principal flow mechanisms.

gas off the vulnerable rotating components. The cooling air returns to the main turbine gas path through a rim seal clearance. Use of excessive cooling air will result in additional losses, which will reduce the efficiency of the gas turbine. Figure 1 illustrates a typical rim seal configuration in an axial turbine stage and principal flow mechanisms affecting the rim seal flows. Rotationally driven and pressure-driven ingestion have been reviewed and considered in correlation models for sealing effectiveness [12,13]. Rotationally driven ingestion is associated with the disk pumping effect, while pressure-driven ingestion is related to the pressure asymmetry caused by vanes and blades in the main gas path. In addition to these mechanisms many recent studies, reviewed in Ref. [11], report large-scale unsteady flow modes with characteristic frequencies unrelated to those of the rotating blade in the main annulus. In the presence of the intrinsic unsteady flow modes empirical correlations and Reynolds-averaged Navier-Stokes (RANS) models give solutions for sealing effectiveness that depart from the experimental measurements [14,15].

The first published experimental observation of these large-scale unsteady flow modes was reported by Cao *et al.* [16] in 2003. Since then a number of experimental and numerical investigations have reported evidence of large-scale unsteady flow modes. Many researchers have postulated the mechanisms of these flow modes, with the Taylor-Couette (T-C) instability and the Kelvin-Helmholtz (K-H) instability being proposed as driving mechanisms. Those proposing the T-C instability include Boudet *et al.* [17], O'Mahoney [18] and Gao *et al.* [19], and those proposing the K-H instability include Rabs *et al.* [20], Chilla *et al.* [21], Savov *et al.* [22], and Horwood *et al.* [15]. Another possible source of unsteadiness, suggested by Berg *et al.* [23], are the Helmholtz and shallow cavity modes.

In Boudet *et al.*'s study [17], unsteady RANS (URANS) solutions showed unsteady flow modes at a low cooling flow condition. It was suggested that centrifugal force and pressure gradient dominated the flow, satisfying the condition for the T-C instability. However, no further evidence was given. Gao *et al.* [19] showed evidence of T-C like vortices using large-eddy simulation (LES) on a similar rim seal configuration. O'Mahoney *et al.* [18] compared URANS and LES solutions of a chute rim seal and suggested the flow behaves in a similar way to a Couette flow system.

Rabs *et al.* [20] conducted URANS simulations on the rig presented by Jakoby *et al.* [24]. In their study a 22.5° sector, smaller than the extent of one lobe of the flow structure reported by Jakoby *et al.* [24], was used for both models with and without vanes and blades. They showed

some similarities of the instantaneous flow field in the rim seal with a shear layer flow model, and suggested that the K-H instability dominates the flow modes. It should be noted that no direct comparison with the experimental results, in terms of the frequency of the flow modes, was presented. Chilla *et al.* [21] presented URANS studies for a typical rim seal configuration, with comparisons to experimental data in the main annulus. By decreasing the difference in tangential velocity between the rim seal flow and the main annulus flow, the unsteadiness was suppressed, in agreement with the flow behavior for the K-H instability. Similar observations were reported by Savov *et al.* [22] through experimental studies. Increasing the difference in tangential velocity at the rim seal leads to greater unsteadiness. Horwood *et al.* [15] studied the unsteady flow modes in a rim seal geometry through experimental and numerical results. In agreement with Rabs *et al.* [20] and Chilla *et al.* [21], they showed the flow unsteadiness amplifying with the increase of the velocity deficit in the rim seal. They also presented instantaneous flow structures, with URANS solutions, showing similarities with the K-H roll-up, but the number of the vortices coincided with the blade count. Berg *et al.*'s study [23] associated the distinct frequencies with the shallow cavity modes and the Helmholtz modes. Though this was supported by analyses of experimental data, the possibility that the unsteady flow features are circumferentially distributed and that the flow structure is rotating were not considered.

In reviewing the studies discussed above we note considerable discrepancies between URANS simulations and the corresponding experimental measurements, and experimental results only give indirect evidence of the flow mechanisms involved. Recent studies using LES have shown improved agreement with experimental measurements to those with RANS and URANS, in terms of pressure distribution and sealing effectiveness. These include studies by O'Mahoney *et al.* [18,25], Gao *et al.* [19], and Pogorelov *et al.* [26]. This indicates that LES can give further insight into flow mechanisms in rim seals.

The present work uses a high-order spectral-element-Fourier method to study the flow mechanisms in turbine rim seal flows, for three typical rim seal configurations. Section II gives a brief description of inertial waves. Section III introduces the three turbine rim seal configurations studied. The numerical method used in this work is presented in Sec. IV. Results and evidence of inertial waves are discussed in Sec. V. Section VI summarizes the main findings.

II. INERTIAL WAVES

Inertial waves, existing in the interior of rotating flows, are induced by the rotation and associated with the restoring effect of Coriolis forces. Such waves can be identified in solutions of the inviscid linearized Navier-Stokes equations in a rotating frame of reference [1].

Considering an incompressible formulation in a relative frame of reference rotating at an angular speed Ω_{rel}, the dimensional Navier-Stokes equations can be expressed in Eqs. (1) and (2). Merging the centrifugal term into the pressure term (p), a reduced pressure can be obtained, $P = p - 0.5\rho(\mathbf{\Omega}_{\mathrm{rel}} \times \mathbf{r})^2$. ρ, $\mathbf{\Omega}_{\mathrm{rel}}$ and $\mathbf{r}$ are density, vector of relative angular speed, and vector of radius, respectively.

$$\mathbf{\nabla} \cdot \mathbf{u} = 0, \tag{1}$$

$$\frac{\partial \mathbf{u}}{\partial t} + \mathbf{u} \cdot \mathbf{\nabla} \mathbf{u} = -\frac{\mathbf{\nabla} p}{\rho} + \nu \mathbf{\nabla} \times (\mathbf{\nabla} \times \mathbf{u}) - 2\mathbf{\Omega}_{\mathrm{rel}} \times \mathbf{u} - \mathbf{\Omega}_{\mathrm{rel}} \times (\mathbf{\Omega}_{\mathrm{rel}} \times \mathbf{r}), \tag{2}$$

where ν is kinematic viscosity.

Letting $\Omega_{\mathrm{rel}}^{-1}$, L, U, Ω_{rel}, and $\rho\Omega_{\mathrm{rel}}UL$ be the reference scales for time, length, velocity, angular speed, and pressure, nondimensional Navier-Stokes equations can be derived as follows:

$$\check{\mathbf{\nabla}} \cdot \check{\mathbf{u}} = 0, \tag{3}$$

$$\frac{\partial \check{\mathbf{u}}}{\partial \check{t}} + \mathrm{Ro}\,\check{\mathbf{u}} \cdot \check{\mathbf{\nabla}} \check{\mathbf{u}} = -\check{\mathbf{\nabla}} \check{P} - \frac{1}{\mathrm{Re}} \check{\mathbf{\nabla}} \times (\check{\mathbf{\nabla}} \times \check{\mathbf{u}}) - 2\hat{\mathbf{i}} \times \check{\mathbf{u}}, \tag{4}$$
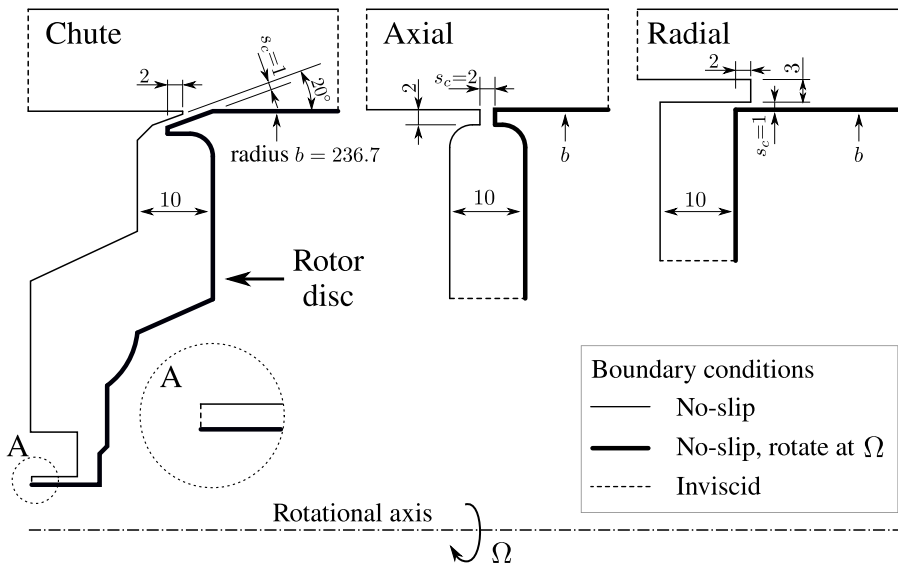
FIG. 2. Schematics of three typical rim seal configurations. Geometrical parameters are in millimetres, and the surfaces of rotating components are highlighted with thick solid lines.

where $\hat{\mathbf{i}}$ is the unit vector along the axis of rotation. Two nondimensional parameters emerge in the momentum equation, which are Rossby number,

$$\mathrm{Ro} = \frac{U}{\Omega_{\mathrm{rel}}L}, \tag{5}$$

and Reynolds number,

$$\mathrm{Re} = \frac{\Omega_{\mathrm{rel}}L^2}{\nu}. \tag{6}$$

If the relative fluid motion is significantly smaller than the rotation of the reference frame and the viscous effect is negligible, i.e., $\mathrm{Ro} \ll 1$ and $\frac{1}{\mathrm{Re}} \ll 1$, then the momentum equation in Eq. (4) may be reduced to

$$\frac{\partial \check{\mathbf{u}}}{\partial \check{t}} = -\check{\boldsymbol{\nabla}} \check{P} - 2\hat{\mathbf{i}} \times \check{\mathbf{u}}. \tag{7}$$

In the steady state Eq. (7) describes the geostrophic mode, where the pressure gradient is exactly balanced with the Coriolis force, i.e., $2\hat{\mathbf{i}} \times \check{\mathbf{u}} = -\check{\boldsymbol{\nabla}} \check{P}$.

For a time-dependent, linear and inviscid fluid governed by Eq. (7) wavelike solutions can be assumed. Greenspan [1] proved that the characteristic frequency of an inertial wave must be between $-2f_{\mathrm{rel}}$ and $2f_{\mathrm{rel}}$, i.e., $|f^*/f_{\mathrm{rel}}| \leqslant 2$, where $f_{\mathrm{rel}} [= \Omega_{\mathrm{rel}}/(2\pi)]$ is the frequency of the relative frame of reference rotating at an angular speed Ω_{rel} about the rotational axis.

III. RIM SEAL CONFIGURATIONS STUDIED

Three typical turbine rim seal configurations—chute, axial, and radial—are considered in this study. Schematics and some geometrical parameters are shown in Fig. 2. The chute seal configuration reproduces the experimental rig studied by Beard *et al.* [27]. The axial seal geometry considers the studies by Gentilhomme *et al.* [28] and Boudet *et al.* [14], but with a larger disk rim radius identical to the chute seal configuration. The radial seal has the same disk rim radius as for the other two seals. All configurations are without vanes and blades in the main gas path, focusing

TABLE I. Rossby number and Reynolds number values in rotating frames of reference for consideration of inertial waves and seal clearance-based Reynolds number.

Seal type	Rossby number (Ro)	Reynolds number (Re)	Reynolds number (Re_{sc})
Chute	0.0598	1.26×10^6	1.11×10^4
Axial	0.137	1.10×10^6	2.21×10^4
Radial	0.0415	1.27×10^6	1.11×10^4

on the intrinsic unsteady flow features. Compared to the chute seal smaller rim cavities, with similar cavity volumes, are used in axial and radial seals, aiming to reduce computational costs. This is considered reasonable as no resonance effects between the rim and inner cavities were identified in the experimental and numerical studies [19,29,30]. The surfaces of the rotor discs are highlighted with thick solid lines in the figure, and they spin at 7000 rpm about the rotational axis, giving a rotational Reynolds number $\mathrm{Re}_\phi = \Omega b^2/\nu = 2.6 \times 10^6$ based on the disk rim radius b and angular speed Ω. Note that a 2-mm seal gap (s_c) is considered for the axial seal, whilst 1-mm seal clearances are used in chute and radial seals. This is relevant in engines, because the relative movements in the axial direction are usually greater than those in the radial direction. To minimize the possible effects of the circumferentially periodic boundary conditions [19,31] and considering the computing capabilities, the sector size is set to $60°$ in the azimuthal direction.

The reference scales and the Rossby and Reynolds numbers for consideration of inertial waves, in Eq. (4), are calculated *a posteriori* with LES solutions. The length scale is the disk rim radius b, as given in Fig. 2, for all three configurations. The rotational speed of the relative frame of reference takes the values of $R_s\Omega$, where values of the swirl ratio R_s are given in Table II. The reference velocity U considers the maximum mean ingestion and egestion velocity, as shown in Fig. 6, which are $\sim$5 m/s, $\sim$10 m/s and $\sim$4 m/s for the chute, axial, and radial seals. These lead to the two nondimensional parameters given in Table I. The Reynolds number based on the disk rim speed and seal clearance, $\mathrm{Re}_{sc} = \Omega b s_c/\nu$, is also given in the table.

IV. METHODOLOGY

A high-order spectral-element-Fourier code, Semtex [32], is used in this study. This solves the nondimensional incompressible Navier-Stokes equations in a stationary frame of reference, as given in Eqs. (8) and (9), using Ω^{-1}, b, Ωb, and $\rho\Omega^2 b^2$ as reference scales for time, length, velocity, and pressure. The choice of this solver is based on its computational efficiency and the fact that the compressibility effects are small for the conditions considered in this paper. This solver uses quadrilateral spectral elements on a meridional semi-plane and Fourier expansions in the third direction. Therefore, the third direction has to be homogeneous or periodic, which is the case for the azimuthal direction in the present study. Within each element high-order Gauss-Lobatto-Legendre Lagrange polynomial interpolants are employed to achieve spectral accuracy. A second-order, semi-implicit, stiffly stable scheme [33] is used for temporal interpolation. For the problems in this study, direct numerical simulation is not feasible due to the high rotational Reynolds number considered. However, the spectral vanishing viscosity technique (SVV) [34], which adds a prescribed amount of artificial viscosity to the momentum equation, is used to model the dissipation effect and to stabilize the calculation. This can be considered as an implicit LES. The Semtex solver and its LES using SVV have been validated in a number of applications, and recently have been successfully implemented in the simulations of gas turbine internal air systems [35–37].

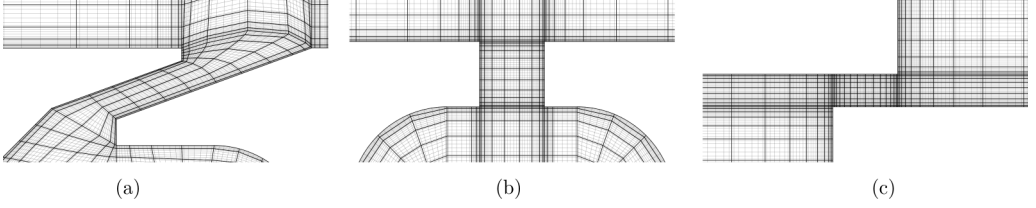$$\check{\nabla} \cdot \check{\mathbf{u}} = 0, \tag{8}$$

FIG. 3. Meshes at the rim seal clearances. Dark lines correspond to elements. Gray lines represent polynomial submeshes. (a) Chute seal, (b) Axial seal, and (c) Radial seal.

$$\frac{\partial \check{\mathbf{u}}}{\partial \check{t}} + \check{\mathbf{u}} \cdot \check{\nabla} \check{\mathbf{u}} = -\check{\nabla} \check{p} + \frac{1}{\mathrm{Re}_\phi} \check{\nabla}^2 \check{\mathbf{u}}. \tag{9}$$

The computational domains of the three configurations in the present study are given in Fig. 2. Zoomed views of the grids at the seal gap are shown in Fig. 3. Dark lines indicate elements, while light gray lines represent high-order polynomial submeshes within each element. The numbers of elements on the meridional planes are 1343, 1139, and 1330 for the chute, axial, and radial seal grids, respectively. The polynomial order of 7 is adopted for all three configurations. In the circumferential direction 1024 Fourier planes are used for the 60° sectors.

Sealed conditions are applied to all three configurations as shown in Fig. 2, i.e., no inlets and outlets. No-slip wall boundary conditions are defined for both rotating and stationary components. A constant angular speed 7000 rpm is set for the rotor disk (represented by thick solid curves) whilst zero velocity is specified to stationary components (shown by thin solid curves). The boundaries that would normally be inlets and outlets in an experiment, denoting by dashed lines in Fig. 2, are treated (with symmetry boundary conditions) as inviscid walls.

The mesh resolution is evaluated, for example, in the seal between the main annulus and the rim cavity, as shown in Fig. 4. The mesh resolutions are calculated for the wall-normal direction (Δy^+, i.e., $\Delta y^+ = u_\tau \Delta y / \nu$), the direction parallel to the seal geometry in the azimuthal plane (Δs^+) and the circumferential direction [$\Delta(r\theta)^+$]. u_τ is the friction velocity. Some wiggles can be seen on the plots, because the values are taken on the polynomial nodes which are expanded within each element. In the three geometries Δy^+ on the first layer of the grid is ~1 at both the stationary and rotating component walls within the seals. For the direction parallel to the seal geometry Δs^+ is less than 40 in the chute seal, and is less than 20 in the axial and radial seals. Similar $\Delta(r\theta)^+$ is found for the three cases, which is between 60 and 100. These mesh resolutions are generally accepted for LES. Given that high-order schemes are used the resolution is considered sufficient.
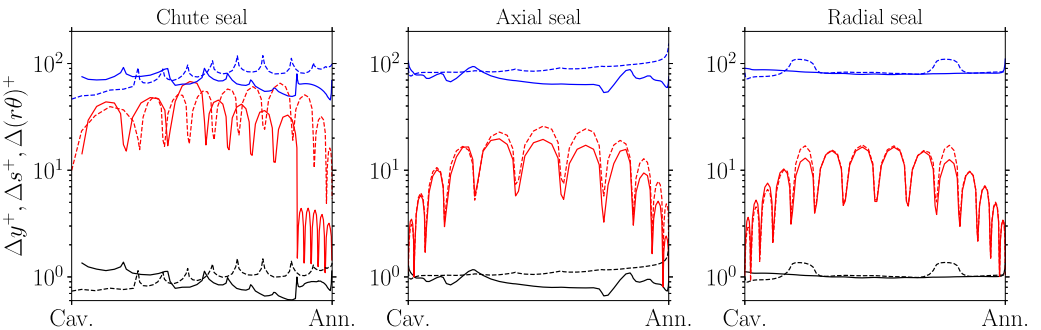

FIG. 4. Mesh resolutions at the seal clearances. Black: Δy^+. Red: Δs^+, i.e., the direction parallel to the seal geometry in the meridional plane. Blue: $\Delta(r\theta)^+$. Solid curves: stationary component side. Dashed curves: rotating component side. Cav.: cavity. Ann.: annulus.
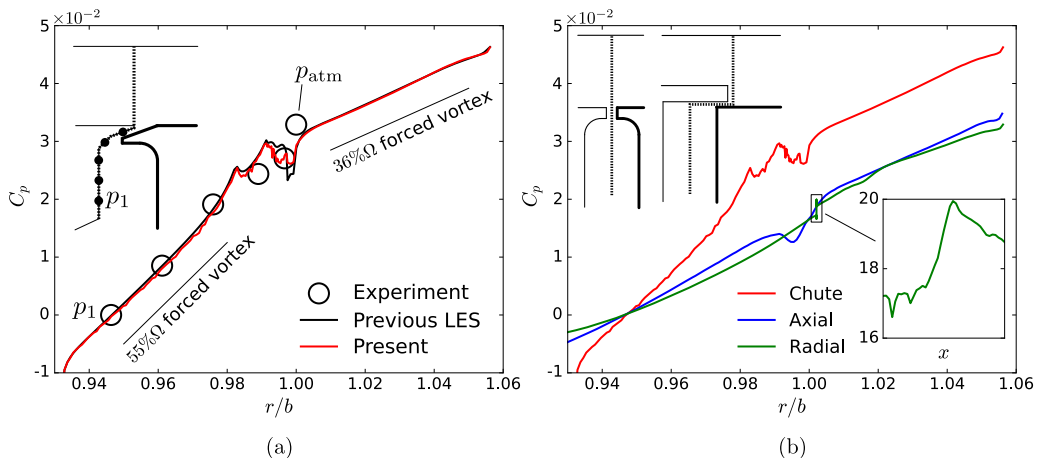
FIG. 5. Mean pressure distribution. (a) Comparison of Semtex, previous LES solution [30], and experimental results [27] for the chute seal configuration. (b) Semtex solutions for the three seal types. r is the local radius, and x is the axial position.

V. RESULTS AND DISCUSSION

A. Mean pressure distribution

As an initial step the mean static pressure coefficient C_p predicted by Semtex for the chute seal is compared with experimental measurement [27] and previous LES from a compressible flow finite volume code [30]. The mean static pressure coefficient is defined as the ratio between the pressure difference to p_1, whose location is shown in the inset of Fig. 5(a), and the dynamic head at the disk rim, as in Eq. (10). The comparison is shown in Fig. 5(a), where the experimental sensors are indicated on the stator disk and the numerical sampling line is represented by the dotted line. Good agreement is achieved among the results. Note that p_{atm} is experimentally measured in the main annulus, its horizontal coordinate on the graph does not correspond to its measurement location.

$$C_p = \frac{\overline{p} - p_1}{0.5\rho(\Omega b)^2}. \tag{10}$$

In Fig. 5(b) mean pressure distributions are compared for the present Semtex solutions. The numerical sampling lines are again indicated with the dotted lines shown in the inset. The pressure distributions are plotted such that p_1 and its location are taken as reference. A steeper curve is observed in the rim cavity for the chute seal, indicating a stronger vortex. This is associated with the cavity geometry of the chute seal. Regarding the axial and radial seals, similar vortex strengths are obtained in the cavity and the main annulus. A subplot illustrates the pressure drop in the axial direction for the radial seal. Clearly a smaller pressure gradient is shown in the radial seal, as the radial pressure gradients in the axial and chute seal must balance the centrifugal force.

B. Mean streamwise velocity

The rim seal flow is dominated by the unsteady effects [19]. But it is still of interest to evaluate the mean velocity through the seal. In this regard the mean streamwise (in parallel with the seal geometry on a meridional plane) velocity profiles within the seal overlapping region are plotted in Fig. 6. Also plotted are indicative streamlines, arrowed curves, for the cavity and the main annulus. The three subplots have the same scales in geometry and velocity magnitude, allowing for direct comparison. Gap recirculation is observed in all seals. The plots also show that the mean ingestion
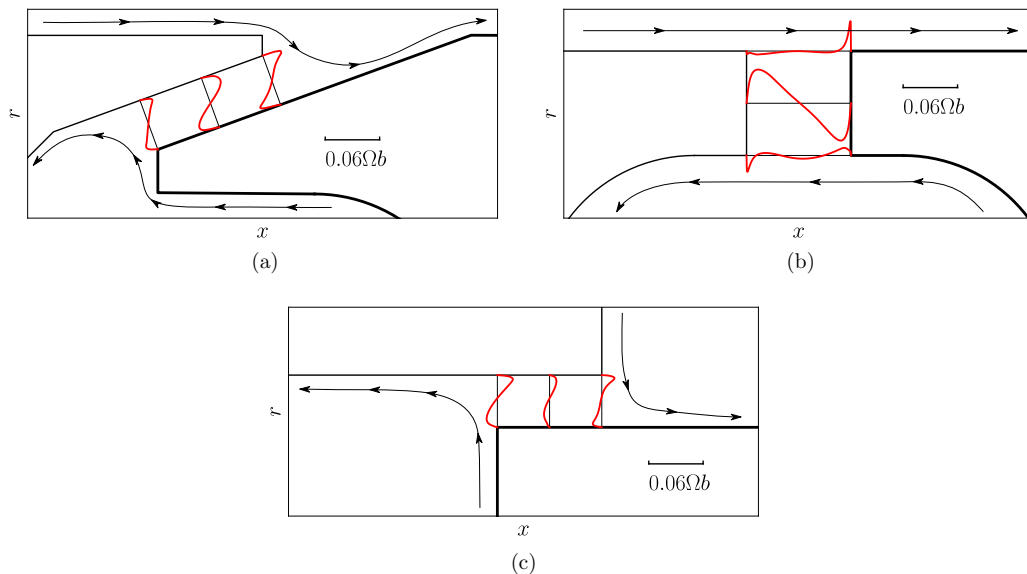
FIG. 6. Mean streamwise (in parallel with the seal geometry on a meridional plane) velocity profiles within the seal overlap. (a) Chute, (b) Axial, and (c) Radial.

takes place near the rotor discs, whereas the mean egestion occurs near the stationary components. The typical Taylor-Couette vortex pair expected for the radial seal is not seen, probably due to the small aspect ratio of the overlap to the seal gap.

C. Characteristics of the unsteady flow structures

High-frequency pressure data are recorded using stationary numerical sensors shown in the insets in Fig. 7. The outermost numerical probe of each seal configuration is placed within the seal overlapping zone. The fast Fourier transform (FFT) is applied to the unsteady pressure data, and the results are plotted in Fig. 7. For the chute seal in subplot (a) distinct peaks are captured by the outermost numerical sensor, within the seal overlapping region. Compared with Gao *et al.*'s solution with a $13.33°$ sector [19], more peaks are observed, showing some similarity with the broadband frequency found in the experiment [27]. Moving radially inboard the distinct peaks reduce and disappear, as is consistent with the observation made with Gao *et al.*'s LES results [30]. In the axial seal, as shown in Fig. 7(b), the pressure signal shows less intense unsteadiness within the seal. This may be associated with the wider seal gap used to accommodate larger relative movement of the engine components in the axial direction. As with the chute seal, no distinct peak is detected with the numerical sensors in the rim cavity. In the subplot (c) the FFT of the pressure signal is shown for the radial seal. In contrast to the other seals, no distinct peak is captured, even within the seal clearance.

The frequencies of the two strongest peaks in the chute and axial seals are normalized with the disk frequency and given in Table II. To derive the characteristics of the unsteady flow structure, an additional numerical sensor was placed at the same axial and radial position as the sensor within the seal (shown in Fig. 7) but with $5°$ spacing in the circumferential direction. The data reduction procedures described by Gao *et al.* [19], using cross correlation, are applied to the pressure signals of these two seals, to obtain the characteristics of the unsteady flow structures. The speed of the flow structures normalized with the disk angular speed, the total number of lobes and the extent of each lobe are calculated and given in Table II. Compared with the speed of the flow structures $\omega_s/\Omega \approx 80\%$ detected in the experiment [27], the speed here
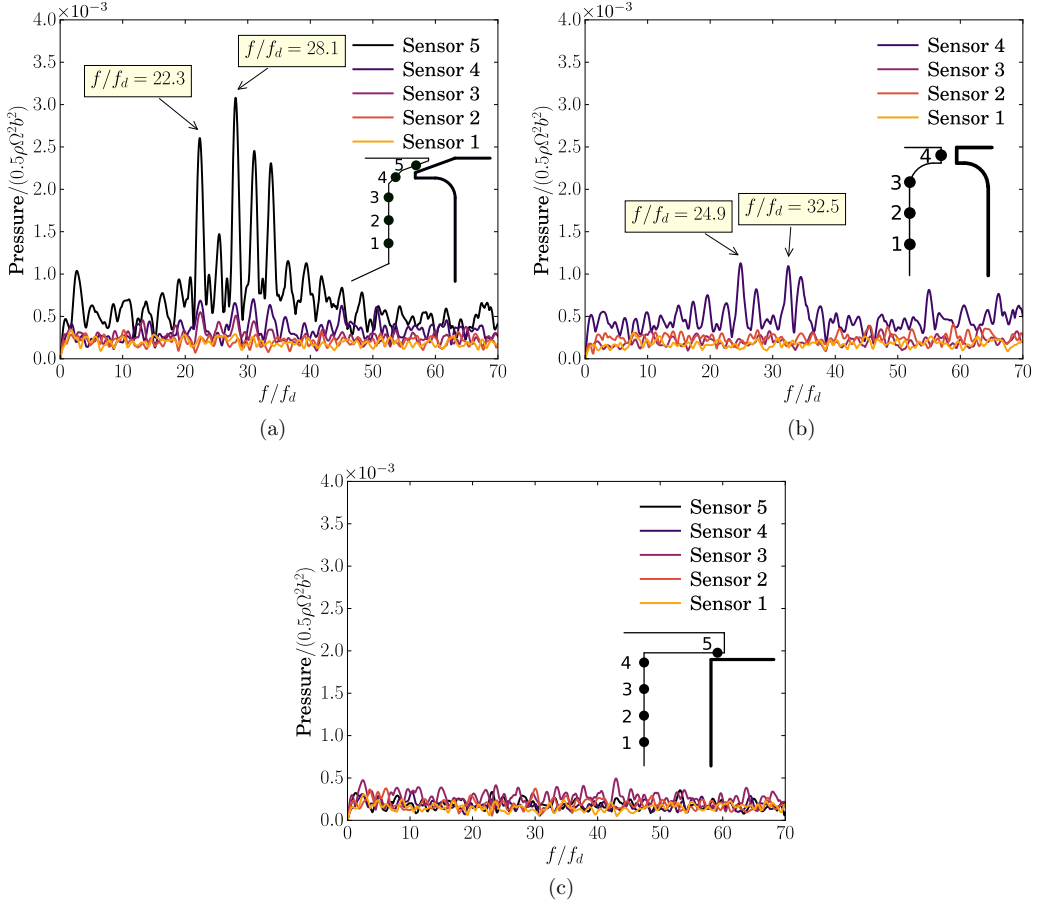
FIG. 7. FFT of unsteady pressure data. f/f_d denotes the frequency normalized with the disk frequency. (a) Chute, (b) Axial, and (c) Radial.

is significantly slower but is in close agreement with the LES solutions obtained earlier [19]. Note that in the axial seal case a lobe angle $4.62°$, less than the sensor spacing, is detected. In this case the second positive cross correlation peak with a positive time lag turns out to be the strongest.

D. Instantaneous flow field

Snapshots of instantaneous flow fields are shown in Fig. 8, extracted on the planes shown in the left insets. These show the swirl ratio $v_\theta/(\Omega r)$. A stronger swirl is shown in the chute rim cavity, associated with the strong vortex observed through the mean pressure coefficient in Fig. 5. Similar swirl levels are observed in the main annulus for the three test cases. Signatures of large-scale unsteady flow structures are observed at the chute and axial seal clearances. Two different views are given for the radial seal, to show the flow field in both the radial and axial directions. The radial seal shows some unsteadiness at the seal region but does not form large-scale flow structures. This is consistent with the FFT results of the pressure signal.

The instantaneous flow structures are also shown on planes across the seal gap, which are made by extruding the middle sampling lines in Fig. 6 in the circumferential direction. The circumferential, streamwise (parallel to the seal geometry in the meridional plane) velocities and

TABLE II. Characteristics of the unsteady flow structures. f/f_d: peak frequency normalized with the disk rotating frequency. ω_s/Ω: speed of the unsteady flow structure normalized with the disk angular speed. N: total number of lobes of the flow structure in a full 360° annulus. β: angle of lobe. $R_s = \overline{v_\theta}/(\Omega r)$: mean swirl ratio of the core flow. $|f^*/f_{\text{rel}}| = (N|\omega_s/\Omega - R_s|/R_s)$: normalized peak frequency of the unsteady flow structure seen in a relative frame of reference rotating at the speed of the mean flow core.

Seal type	f/f_d	ω_s/Ω	N	β [deg]	R_s	$|f^*/f_{\text{rel}}|$
Chute	22.3	47.1%	48	7.5	48.2%	1.10
	28.1	47.2%	60	6		1.24
Axial	24.9	41.3%	60	6	42.1%	1.14
	32.5	41.6%	78	4.62		0.926
Radial	n.a.	n.a.	n.a.	n.a.	48.6%	n.a.

the pressure coefficient for the three seal geometries are shown in Fig. 9, at the same time instant as for Fig. 8. Clear large-scale flow structures are shown through high and low levels of velocity. The boundary layers at both the stationary and rotating component walls can be observed through the circumferential velocity contours. The phase of velocities near the rotating component is in advance of that near the stationary component. The pressure contour shows the same phase across the seal gap. The numbers of lobes in the 60° sector are approximately 8 and 10 for the chute and axial seals, consistent with the results obtained from the unsteady pressure signals. In the radial seal unsteadiness of the circumferential velocity can be observed. The level of ingestion and egestion represented by the streamwise velocity levels is significantly weaker than those for the
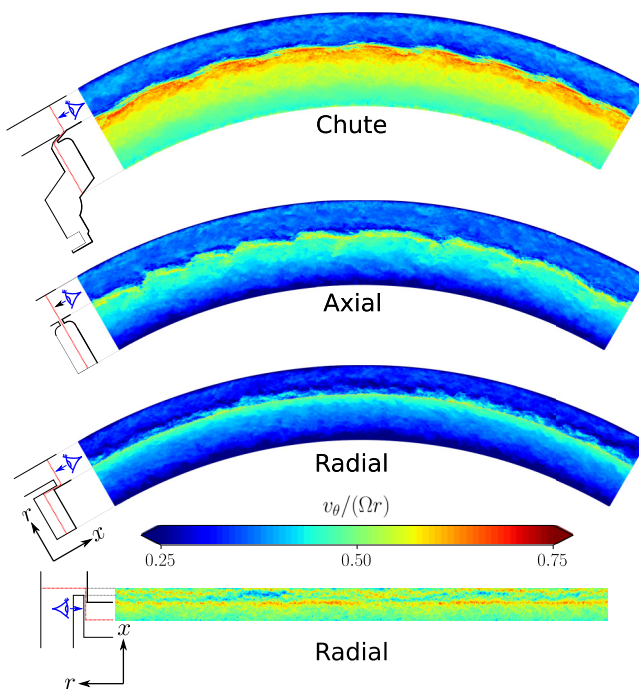

FIG. 8. Instantaneous flow fields illustrated with swirl ratio contours. The extraction planes are given by the left insets.
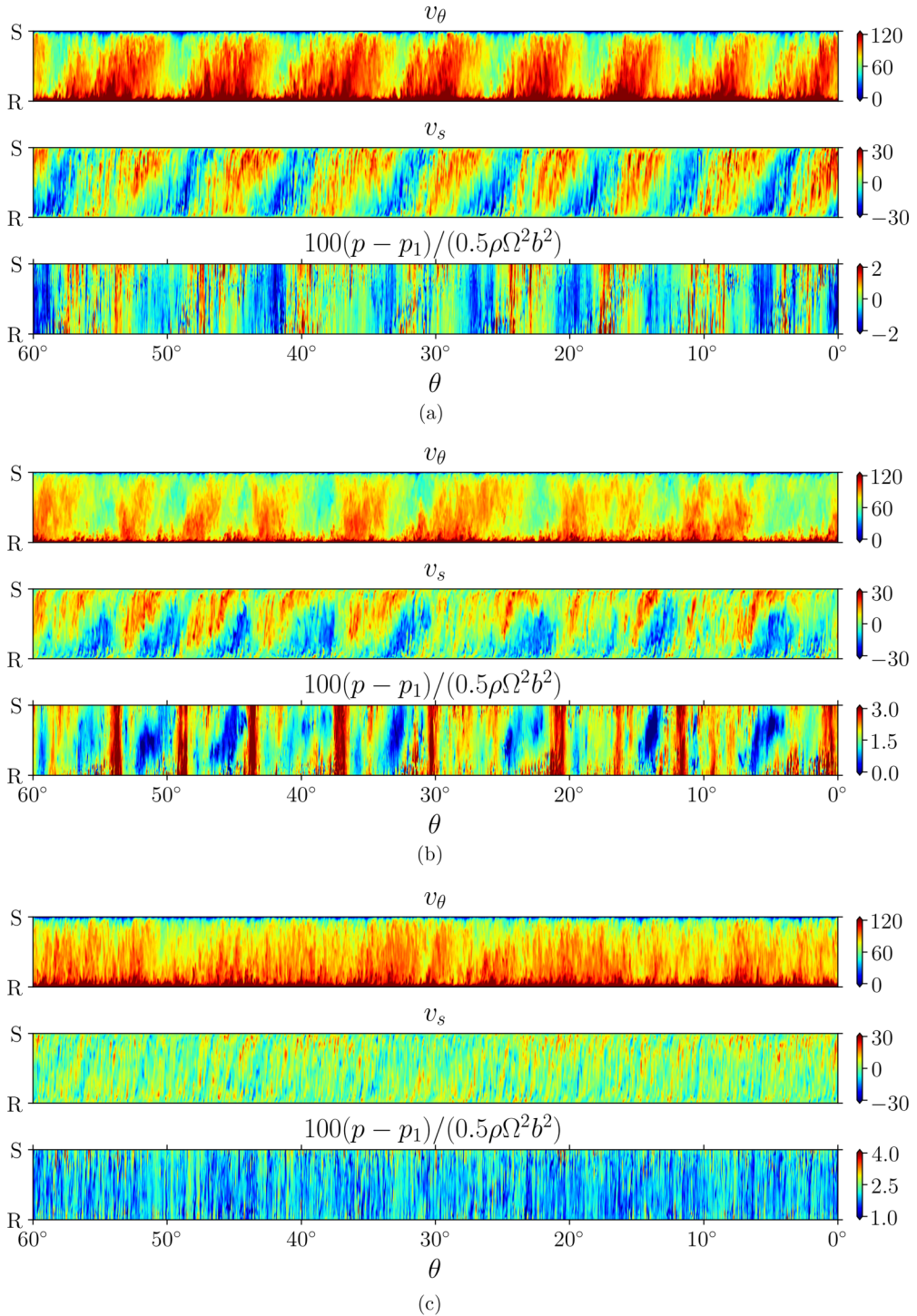
FIG. 9. Instantaneous flow fields illustrated with the circumferential (v_θ), streamwise (v_s, in parallel to the seal geometry) velocities and the pressure coefficient. Sampling planes are constructed by extruding the middle sampling lines shown in Fig. 6. R: rotating component wall. S: stationary component wall. The direction of rotation is from right to left. Velocity units are m/s. (a) Chute, (b) Axial, and (c) Radial.
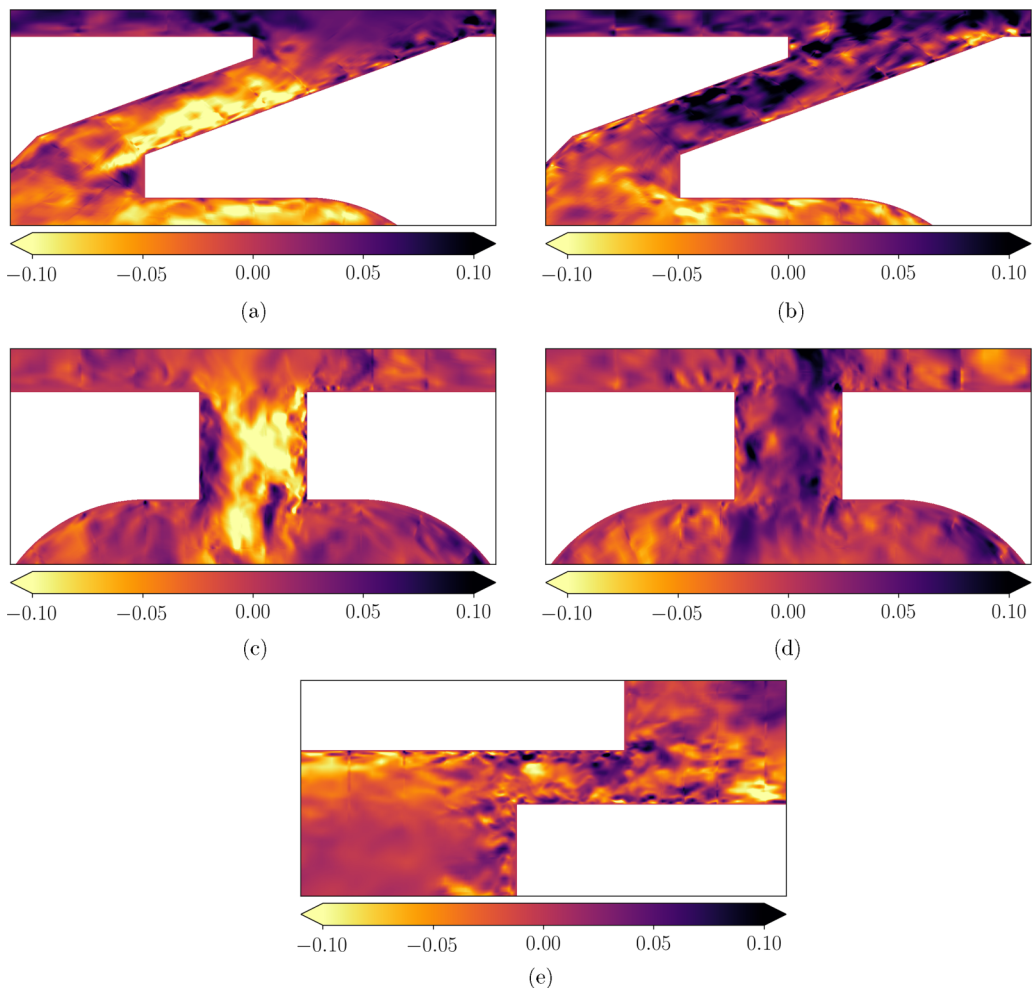
FIG. 10. Instantaneous velocity fields on cross sections at different circumferential positions. The time corresponds to that in Fig. 9. $v_x/(\Omega b)$ and $v_r/(\Omega b)$ represent nondimensional axial and radial velocities. (a) Contour of $v_x/(\Omega b)$ at $\theta = 5°$. Ingestion, (b) Contour of $v_x/(\Omega b)$ at $\theta = 15°$. Egestion, (c) Contour of $v_r/(\Omega b)$ at $\theta = 50°$. Ingestion, (d) Contour of $v_r/(\Omega b)$ at $\theta = 20°$. Egestion, and (e) Contour of $v_x/(\Omega b)$ at $\theta = 30°$.

chute and axial seals. The pressure fluctuation level is also lower than that in the chute and axial seal configurations.

Circumferential cross sections are taken at positions representative of ingestion and egestion for the chute and axial seal configurations, and an arbitrary circumferential cross section is plotted for the radial seal. These are shown in Fig. 10, and the corresponding circumferential position can be seen in Fig. 9. The normalized axial velocity is plotted for the chute and radial seals, representing the ingestion and egestion. For the axial seal the normalized radial velocity is plotted. Clear ingestion and egestion flows are observed in the chute and axial seal gaps. In both sub-figures (a) and (c), ingestion occurs near the rotating components. For the radial seal the magnitude of flow through the seal is much weaker, indicating that the ingestion and egestion are mitigated.

E. Inertial waves

Clear evidence of waves existing within the seal has been shown above. Interaction of ingress and egress flows produces waves for the chute and axial seals for which the radial and tangential
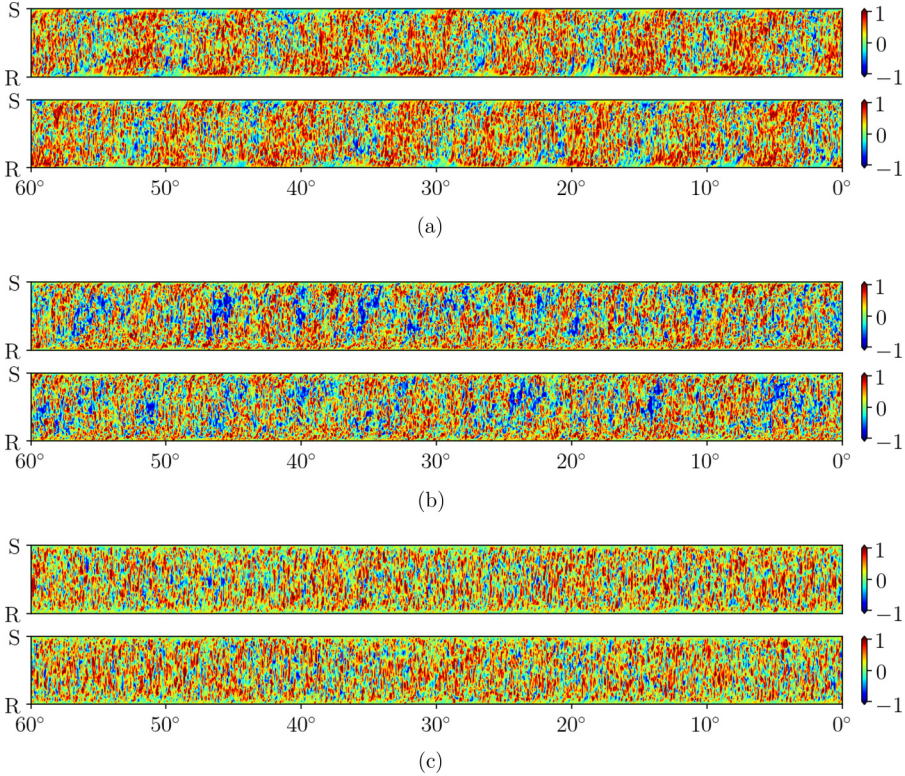
FIG. 11. Instantaneous helicity density $[\mathbf{u} \cdot \boldsymbol{\omega}/(|\mathbf{u}||\boldsymbol{\omega}|)]$ plots in the relative frame of reference rotating with the mean flow core. Contours are taken at two time instants differing by one rotor revolution time. The second plot of each seal is at the same time as results in Fig. 9. Sampling planes are constructed by extruding the middle sampling lines shown in Fig. 6. R: rotating component wall. S: stationary component wall. The direction of rotation is from right to left. (a) Chute, (b) Axial, and (c) Radial.

momentum equations are strongly coupled through the Coriolis terms. In the radial seal geometrical restrictions suppress the radial velocity and Coriolis force, and no waves are observed. This suggests that the large-scale flow structures observed can be classed as inertial waves. Further details of the waves and some comparison with the inertial wave theory are given in this section.

The angular speed of the mean flow core, represented by mean swirl ratio R_s, within each seal is computed and listed in Table II. The mean angular speed of the flow core is close to that of the unsteady flow structures ω_s/Ω, as given in the same table.

The peak frequency of the unsteady flow structures is obtained through FFT of the stationary pressure probe data. Normalisation of this frequency with the disk frequency f_d, say f/f_d, has a physical meaning: the lobe number of the flow structure seen by a stationary probe as the rotor disk travels one rotor revolution. Therefore, this normalized frequency (f/f_d) is equal to the product of the total lobe number N and the normalized angular speed of the flow structure ω_s/Ω: $f/f_d = N\omega_s/\Omega$. The number of lobes (f^*/f_d) seen in the relative frame of reference rotating at the speed of the mean flow core (Ω_{rel}) during one rotor revolution is equal to the product of N and the relative speed of the wave to the mean flow core $[(\omega_s - \Omega_{\text{rel}})/\Omega]$: $N(\omega_s - \Omega_{\text{rel}})/\Omega$. The inertial wave frequency (f^*/f_{rel}) in the relative frame of reference of the mean flow core is the lobe number seen as this frame of reference travels one revolution, which is $N(\omega_s - \Omega_{\text{rel}})/\Omega_{\text{rel}}$. As $\Omega_{\text{rel}} = R_s\Omega$, one can derive $f^*/f_{\text{rel}} = N(\omega_s/\Omega - R_s)/R_s$.
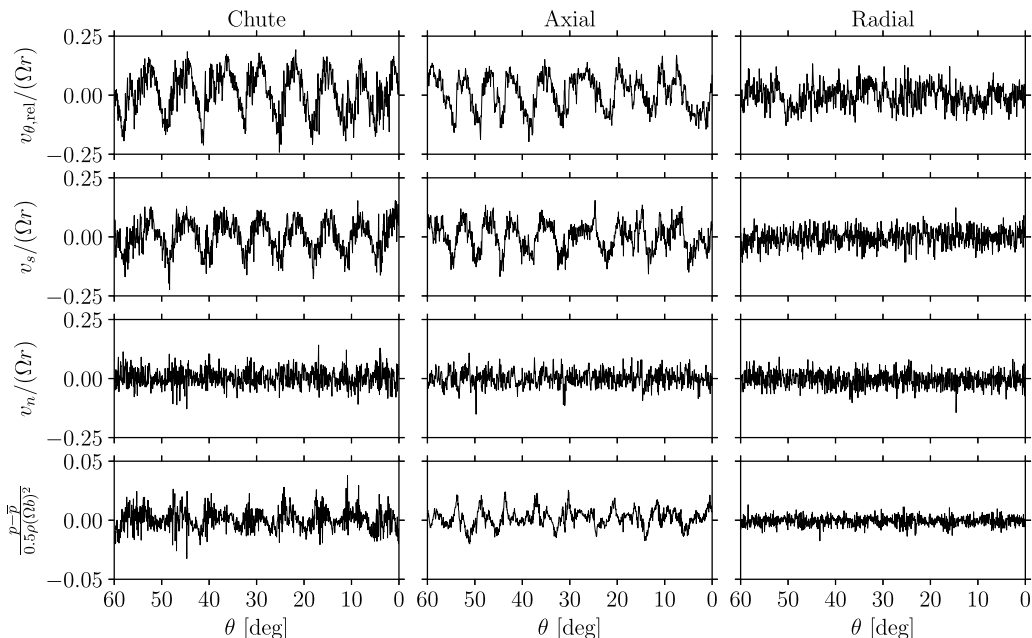
FIG. 12. Instantaneous velocities in the relative frame of reference rotating with the mean flow core. Samples are taken at the center between the stationary and rotating components in Fig. 9. The direction of rotor's movement is from right to left.

These frequencies, as given in Table II, are between 0.926 and 1.24, satisfying the theoretical limits $|f^*/f_{\mathrm{ref}}| \leqslant 2$ for small amplitude inertial waves as shown by Greenspan [1]. Use of $60°$ sectors may impose restrictions for inertial wave development. Inspection of our previous LES data [30] on the chute seal configuration with $13.3°$ and $24.8°$ sectors (1/27 and 2/29 of the full annulus) indicates inertial waves with wave numbers between $43 − 81$ rotating at 43–45% of the rotor speed. This corresponds to relative frequencies f^*/f_{rel} between 0.497 and 1.73, within the range for inertial waves.

Flows dominated by inertial waves are helical, as discussed by Galtier [38] and Chen *et al.* [39]. Figure 11 shows instantaneous helicity density $[\mathbf{u} \cdot \boldsymbol{\omega}/(|\mathbf{u}||\boldsymbol{\omega}|)]$ contours in the relative frame of reference rotating with the mean flow core, where $\boldsymbol{\omega}$ is the vorticity vector. Two contour plots are shown for each seal at time instants differing by one rotor revolution time, and the second time instant corresponds to that considered in Fig. 9. Large-scale flow patterns are observed in the chute and axial seal configurations. Ingestion is associated with positive helicity flow, while egestion is related to negative helicity flow. The helicity reflected flow structure is less clear for the radial seal.

The instantaneous flow solutions are further illustrated in Fig. 12 by line plots midway between the stationary and rotating component walls from the flow fields shown in Fig. 9. The relative circumferential velocity ($v_{\theta,\mathrm{rel}}$) is obtained in the relative frame of reference rotating with the mean flow core. Velocity fluctuations associated with large-scale flow structures are observed in the chute and axial seals. In the chute seal high amplitude velocity fluctuations are shown in the circumferential and the streamwise directions, with a limited wall-normal component (v_n) due to the seal geometry restricting the flow. In the axial seal, the wall-normal velocity component is restricted and high amplitude velocity fluctuations are seen in the circumferential and streamwise directions. Similar fluctuations are shown for the pressure. The chute and axial seals show similar level of streamwise velocity fluctuations. In the radial seal some fluctuations can be observed in the circumferential direction but no large-scale flow features are identified in the streamwise direction, which is the direction associated with ingestion and egestion.
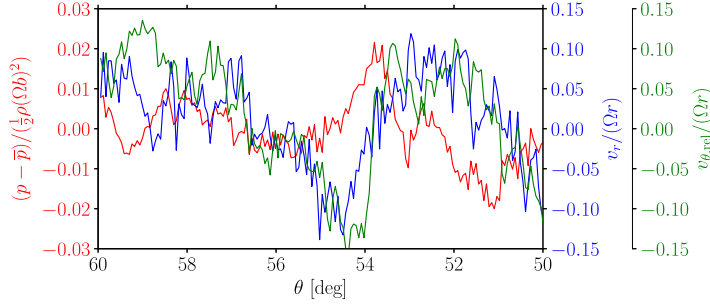
FIG. 13. Instantaneous relative tangential and radial velocities, and pressure for the axial seal. Zoomed view of data shown in Fig. 12 between $\theta = 50°$ and $60°$. Flow moves from right to left.

Figure 12 also shows the relation between the phases for the velocity and pressure fluctuations. An example is given with the solution of the axial seal configuration in Fig. 13 for a $10°$ circumferential sector. The relative tangential and radial velocities, and the pressure coefficient are plotted together. The flow travels from right to left. The two velocity signals are in-phase, and are out-phase with the pressure signal. A phase advance is seen on the pressure signal compared to the velocity. The phase analysis between the velocities and pressure is also confirmed by cross correlation of signals obtained at different time instants, following the method described by Gao *et al.* [19]. The two velocity components are in-phase, while the pressure has a $\sim 1°$ phase difference with the velocities, as can be seen in Fig. 13. This phase difference corresponds to $\sim 1/6$th of the azimuthal extent of the wave at the most prominent frequency of $f/f_d = 28.1$. Similar analysis was applied to the previous LES results by Gao *et al.* [30] for the $24.8°$ sector chute seal configuration, showing the same results in terms of the phase difference between the velocity components and the pressure.

An interpretation of the flow field is shown in Fig. 14. This is in the relative frame of reference rotating with the mean flow core. Egestion occurs downstream of a low pressure region and upstream of a high pressure region. The flow moves faster than the mean flow in the circumferential direction as egestion takes place. At the position where egestion occurs both the pressure force F_p and the Coriolis force F_{Cor} are in the opposite direction to the rotation. Assuming in the relative frame of reference rotating with the mean core flow, the Rossby number is sufficiently small and the rotational Reynolds number is sufficiently large, the linearized momentum equation for inertial wave in Eq. (7) applies. This implies that the Coriolis force and the pressure force have to be balanced by the time derivative of the velocity, satisfying the condition for an inertial wave. Furthermore, in the radial
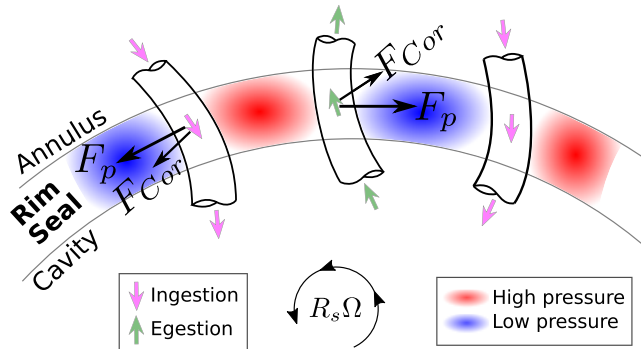

FIG. 14. Schematic of ingestion and egestion flow through rim seal affected by an inertial wave.

seal the radial movement of the flow is restricted by the seal geometry, so there is no contribution from Coriolis force in the tangential direction. The inertial wave is suppressed as expected, as shown in Figs. 7–12.

Though inertial waves have been identified in differentially rotating systems such as the work of Rieutord and Valdettaro [8], the gap between the inner and outer rotating surfaces in these cases are sufficiently large to accommodate radial motion of the fluids. In the radial seal configuration of the present study the ratio between the gap and inner cylinder radius is ∼0.004, sufficiently small to confine the radial fluid motion and thus suppress the inertial wave.

The flows within the seal gaps are expected to be turbulent subjected to high flow shears near the solid walls, shear between the ingress and egress streams, and transport of turbulence from cavity and annulus flows. The turbulence and boundary conditions for the rim seal flow may be expected to modify the inertial waves predicted by classical theory, but the susceptibility to waves clearly remains.

VI. CONCLUSIONS

Numerical studies have been conducted for three typical turbine rim seal geometries—chute, axial and radial—using large-eddy simulation with a high-order spectral-element-Fourier solver. The use of this incompressible solver is validated against the experimental results and previous LES results with a compressible code, in terms of mean pressure distribution, for a chute type turbine rim seal configuration.

Simplified rim cavities are used for the axial and radial seals, compared to the chute seal geometry. This shows some effects on the forced vortex distribution in the cavity. Within the gap, mean flow recirculation is observed in all the three rim seal configurations. The radial seal does not show the Taylor-Couette vortex pair that might be expected for this configuration, presumably due to the relatively short aspect ratio between the seal overlapping length and the seal gap.

Large scale unsteady flow structures are identified in the chute and axial seals at the seal clearance, rotating at angular speeds close to those of the mean core flow but much smaller than that of the rotor disk. This shows significant difference with the experiments where the flow structures were estimated to rotate at ∼80%Ω, but is in close agreement with the previous LES using a compressible flow solver.

In a relative frame of reference rotating at the mean angular speed of the core flow in the seal the normalized characteristic frequencies are between 0.926 and 1.24, satisfying the theoretical limits for inertial wave, i.e., $|f^*/f_{\rm rel}| \leqslant 2$. The helicity density contour plots, showing large-scale flow patterns, also give evidence that the rim sealing flows are dominated by inertial waves in the chute and axial seals. As confirmed by the cross correlation analysis, velocity fluctuations are in-phase with each other, but are out-phase with the pressure signal for ∼1/6th of a wavelength in the azimuthal direction. This means that the pressure force and the Coriolis force have to be balanced by the time derivative of velocity as in the linearized momentum equation for the inertial wave. In the radial seal configuration, where radial flow motion is restricted by the seal geometry, the Coriolis force in the tangential direction is limited and the inertial wave is suppressed as expected. As turbulence is expected within the seal gap, its effect could modify the inertial wave through the nonlinear term of the momentum equation.

The present results illustrate the nature of the inertial waves and show that they dominate the flow in the axial and chute seals. It has previously been postulated that Taylor-Couette (T-C) and Kelvin-Helmholtz instabilities are driving forces for these waves. Considering the complexity and high Reynolds number of the flow (even in the simplified configurations considered here) it is difficult to relate the results to these classical phenomena. However, the axial seal is not expected to induce T-C instability, so it may be concluded that this is not a requirement for waves to form. Stability analysis considering stable and marginally unstable low Reynolds number flow might give more insight. Further interesting research questions of practical interest include the sensitivity to seal geometry including the chute seal angle and degree of radial overlap required to suppress the inertial waves.

[1] H. P. Greenspan, *The Theory of Rotating Fluids* (Cambridge University Press, Cambridge, 1968).

[2] C. D. Andereck, S. S. Liu, and H. L. Swinney, Flow regimes in a circular Couette system with independently rotating cylinders, J. Fluid Mech. **164**, 155 (1986).

[3] P. Melchior and B. Ducarme, Detection of inertial gravity oscillations in the Earth's core with a superconducting gravimeter at Brussels, Phys. Earth Planet. Inter. **42**, 129 (1986).

[4] K. D. Aldridge and L. I. Lumb, Inertial waves identified in the Earth's fluid outer core, Nature **325**, 421 (1987).

[5] C. Sidi and J. Barat, Observational evidence of an inertial wind structure in the stratosphere, J. Geophys. Res.: Atmos. **91**, 1209 (1986).

[6] C. Garrett and W. Munk, Internal waves in the ocean, Annu. Rev. Fluid Mech. **11**, 339 (1979).

[7] M. H. Alford, J. A. MacKinnon, H. L. Simmons, and J. D. Nash, Near-inertial internal gravity waves in the ocean, Annu. Rev. Marine Sci. **8**, 95 (2016).

[8] M. Rieutord and L. Valdettaro, Inertial waves in a rotating spherical shell, J. Fluid Mech. **341**, 77 (1997).

[9] E. Yarom and E. Sharon, Experimental observation of steady inertial wave turbulence in deep rotating flows, Nat. Phys. **10**, 510 (2014).

[10] J. M. Lopez and P. Gutierrez-Castillo, Three-dimensional instabilities and inertial waves in a rapidly rotating split-cylinder flow, J. Fluid Mech. **800**, 666 (2016).

[11] J. W. Chew, F. Gao, and D. M. Palermo, Flow mechanisms in axial turbine rim sealing, Proc. Inst. Mech. Eng. Part C **233**, 7637 (2019).

[12] B. V. Johnson, G. J. Mack, R. E. Paolillo, and W. A. Daniels, Turbine rim seal gas path flow ingestion mechanisms, in *Proceedings of the 30th Joint Propulsion Conference and Exhibit* (AIAA, Reston, Virginia, 1994), Paper No. 94-2073.

[13] J. A. Scobie, C. M. Sangan, J. M. Owen, and G. D. Lock, Review of ingress in gas turbines, J. Eng. Gas Turbines Power **138**, 120801 (2016).

[14] J. Boudet, V. N. D. Autef, J. W. Chew, N. J. Hills, and O. Gentilhomme, Numerical simulation of rim seal flows in axial turbines, Aeronaut. J. **109**, 373 (2005).

[15] J. T. M. Horwood, F. P. Hualca, J. A. Scobie, M. Wilson, C. M. Sangan, and G. D. Lock, Experimental and computational investigation of flow instabilities in turbine rim seals, J. Eng. Gas Turbines Power **141**, 011028 (2019).

[16] C. Cao, J. W. Chew, P. R. Millington, and S. I. Hogg, Interaction of rim seal and annulus flows in an axial flow turbine, in *Proceedings of the ASME Turbo Expo 2003, collocated with the 2003 International Joint Power Generation Conference* (ASME Press, New York, 2003), Paper No. GT2003-38368.

[17] J. Boudet, N. J. Hills, and J. W. Chew, Numerical simulation of the flow interaction between turbine main annulus and disc cavities, in *Proceedings of the ASME Turbo Expo 2006: Power for Land, Sea, and Air* (ASME Press, New York, 2006), Paper No. GT2006-90307.

[18] T. S. D. O'Mahoney, N. J. Hills, J. W. Chew, and T. Scanlon, Large-eddy simulation of rim seal ingestion, Proc. Inst. Mech. Eng., Part C **225**, 2881 (2011).

[19] F. Gao, J. W. Chew, P. F. Beard, D. Amirante, and N. J. Hills, Large-eddy simulation of unsteady turbine rim sealing flows, Int. J. Heat Fluid Flow **70**, 160 (2018).

[20] M. Rabs, F.-K. Benra, H. J. Dohmen, and O. Schneider, Investigation of flow instabilities near the rim cavity of a 1.5 stage gas turbine, in *Proceedings of the ASME Turbo Expo 2009: Power for Land, Sea, and Air* (ASME Press, New York, 2009), Paper No. GT2009-59965.

[21] M. Chilla, H. Hodson, and D. Newman, Unsteady interaction between annulus and turbine rim seal flows, J. Turbomach. **135**, 051024 (2013).

[22] S. S. Savov, N. R. Atkins, and S. Uchida, A comparison of single and double lip rim seal geometries, J. Eng. Gas Turbines Power **139**, 112601 (2017).

[23] R. A. Berg, C. S. Tan, Z. Ding, G. Laskowski, P. Palafox, and R. Miorini, Experimental and analytical assessment of cavity modes in a gas turbine wheelspace, J. Eng. Gas Turbines Power **140**, 062502 (2018).

[24] R. Jakoby, T. Zierer, K. Lindblad, J. Larsson, L. de Vito, D. E. Bohn, J. Funcke, and A. Decker, Numerical simulation of the unsteady flow field in an axial gas turbine rim seal configuration, in *Proceedings of the ASME Turbo Expo 2004: Power for Land, Sea, and Air* (ASME Press, New York, 2004), Paper No. GT2004-53829.

[25] T. O'Mahoney, N. Hills, and J. Chew, Sensitivity of LES results from turbine rim seals to changes in grid resolution and sector size, Progr. Aerospace Sci. **52**, 48 (2012).

[26] A. Pogorelov, M. Meinke, and W. Schröder, Large-eddy simulation of the unsteady full 3D rim seal flow in a one-stage axial-flow turbine, Flow, Turb. Combust. **102**, 189 (2019).

[27] P. F. Beard, F. Gao, K. S. Chana, and J. W. Chew, Unsteady flow phenomena in turbine rim seals, J. Eng. Gas Turbines Power **139**, 032501 (2016).

[28] O. Gentilhomme, N. J. Hills, A. B. Turner, and J. W. Chew, Measurement and analysis of ingestion through a turbine rim seal, J. Turbomach. **125**, 505 (2003).

[29] A. Bru Revert, P. F. Beard, D. M. Palermo, J. W. Chew, and S. Bottenheim (private communication).

[30] F. Gao, N. Poujol, J. W. Chew, and P. F. Beard, Advanced numerical simulation of turbine rim seal flows and consideration for RANS turbulence modelling, in *Proceedings of ASME Turbo Expo 2018: Turbomachinery Technical Conference and Exposition* (ASME Press, New York, 2018), Paper No. GT2018-75116.

[31] L. Fang, Background scalar-level anisotropy caused by low-wave-number truncation in turbulent flows, Phys. Rev. E **95**, 033102 (2017).

[32] H. M. Blackburn and S. J. Sherwin, Formulation of a Galerkin spectral element-Fourier method for three-dimensional incompressible flows in cylindrical geometries, J. Comput. Phys. **197**, 759 (2004).

[33] G. E. Karniadakis, M. Israeli, and S. A. Orszag, High-order splitting methods for the incompressible Navier-Stokes equations, J. Comput. Phys. **97**, 414 (1991).

[34] G. S. Karamanos and G. E. Karniadakis, A spectral vanishing viscosity method for large-eddy simulations, J. Comput. Phys. **163**, 22 (2000).

[35] D. B. Pitz, O. Marxen, and J. W. Chew, Onset of convection induced by centrifugal buoyancy in a rotating cavity, J. Fluid Mech. **826**, 484 (2017).

[36] D. B. Pitz, J. W. Chew, and O. Marxen, Large-eddy simulation of buoyancy-induced flow in a sealed rotating cavity, J. Eng. Gas Turbines Power **141**, 021020 (2018).

[37] F. Gao, D. B. Pitz, and J. W. Chew, Numerical investigation of buoyancy-induced flow in a sealed rapidly rotating disc cavity, Int. J. Heat Mass Transf. **147**, 118860 (2020).

[38] S. Galtier, Weak inertial-wave turbulence theory, Phys. Rev. E **68**, 015301 (2003).

[39] Q. Chen, S. Chen, and G. L. Eyink, The joint cascade of energy and helicity in three-dimensional turbulence, Phys. Fluids **15**, 361 (2003).